INTERFACE FOCUS

royalsocietypublishing.org/journal/rsfs

Research

Cite this article: Wijeratne PA, Vavourakis V. 2019 A quantitative *in silico* platform for simulating cytotoxic and nanoparticle drug delivery to solid tumours. *Interface Focus* **9**: 20180063.
http://dx.doi.org/10.1098/rsfs.2018.0063

Accepted: 11 February 2019

One contribution of 15 to a theme issue 'Multi-resolution simulations of intracellular processes'.

Subject Areas:
bioengineering, biomechanics, computational biology

Keywords:
in silico model, finite element, cancer simulation, drug delivery, chemotherapy, nanomedicine

Author for correspondence:
Vasileios Vavourakis
e-mail: vavourakis.vasileios@ucy.ac.cy

Electronic supplementary material is available online at https://dx.doi.org/10.6084/m9.figshare.c.4408094.

THE ROYAL SOCIETY PUBLISHING

A quantitative *in silico* platform for simulating cytotoxic and nanoparticle drug delivery to solid tumours

Peter A. Wijeratne[1] and Vasileios Vavourakis[2,3]

[1]Centre for Medical Imaging Computing, Department of Computer Science, and [2]Department of Medical Physics and Biomedical Engineering, University College London, London, UK
[3]Department of Mechanical and Manufacturing Engineering, University of Cyprus, Nicosia, Cyprus

PAW, 0000-0002-4885-6241; VV, 0000-0002-4102-2084

The role of tumour–host mechano-biology and the mechanisms involved in the delivery of anti-cancer drugs have been extensively studied using *in vitro* and *in vivo* models. A complementary approach is offered by *in silico* models, which can also potentially identify the main factors affecting the transport of tumour-targeting molecules. Here, we present a generalized three-dimensional *in silico* modelling framework of dynamic solid tumour growth, angiogenesis and drug delivery. Crucially, the model allows for drug properties—such as size and binding affinity—to be explicitly defined, hence facilitating investigation into the interaction between the changing tumour–host microenvironment and cytotoxic and nanoparticle drugs. We use the model to qualitatively recapitulate experimental evidence of delivery efficacy of cytotoxic and nanoparticle drugs on matrix density (and hence porosity). Furthermore, we predict a highly heterogeneous distribution of nanoparticles after delivery; that nanoparticles require a high porosity extracellular matrix to cause tumour regression; and that post-injection transvascular fluid velocity depends on matrix porosity, and implicitly on the size of the drug used to treat the tumour. These results highlight the utility of predictive *in silico* modelling in better understanding the factors governing efficient cytotoxic and nanoparticle drug delivery.

1. Introduction

The efficient delivery of drugs to solid tumours is determined by a complex system of biophysical factors originating from tumour–host interactions [1–4]. Specifically, growth-induced mechanical stresses exerted by the tumour on the surrounding tissue cause changes in the structure and distribution of the surrounding vasculature, increased interstitial fluid pressure and compromised delivery efficacy [5–7]. These effects occur across multiple length and time scales, with rapid diffusion of single molecule agents—such as cytotoxic drugs—contrasting with convection-dominated transport of larger macromolecules, such as proteoglycans in the extracellular matrix (ECM), and nanoparticles, which have been extensively studied as a potential delivery system for therapeutic drugs [8]. However, progress in developing an effective nanoparticle-based therapy has been slow, largely due to the aforementioned complexity of the tumour–host environment [9]. As such, there is an increasing need for new methodologies that can be used to realistically model tumour–host pathophysiology, and hence estimate the optimal biophysical and material conditions for efficient delivery.

In silico modelling of drug delivery to tumours, whereby the tumour–host system is modelled according to biophysical laws, has been used to predict the effect of blood-borne drugs on pathological tissues. In this paper, we provide an overview of the most recent efforts in this field; for more extensive

reviews, see [3,10]. Broadly speaking, *in silico* models can be split into two categories: (i) static-tissue models, where the tumour and vasculature are treated as a static object *in situ* and drug delivery is modelled as a separate dynamic process; and (ii) dynamic-tissue models, where both the tumour and surrounding tissue dynamics are coupled with drug kinematics. A static-tissue model was employed by D'Esposito *et al.* [11], where the authors found good agreement between model predictions of blood flow and the spatial distribution of drug uptake and data acquired from *in vivo* mouse model images. Sefidgar *et al.* [12] compared models of static and dynamic vascular networks and found that the dynamic network predicted a more heterogeneous and irregular vascular structure than the static network. More recently, Vavourakis and colleagues [13] developed a dynamic-tissue model of solid tumour growth and angiogenesis, which recapitulated the distribution and structure of pathological vascular networks from *in vivo* mouse model images. This framework was then extended to include a model of cytotoxic drug delivery [14], which predicted that chemotherapeutic agents have the highest impact when delivered via highly permeable, dense vascular networks.

Here, we generalize the modelling framework to account for drugs of any size, and in particular nanoparticles. We then use the model to make predictions of the effects of both tumour–host and drug properties on delivery efficiency and distribution. Crucially, our dynamic-tissue approach allows us to model how the tumour–host environment changes with time, and hence make predictions of the resulting vascular and tissue distributions post-therapy. This has particular relevance to staged therapeutic approaches, where drugs or combinations of different drugs are administered at intervals in an attempt to maximize delivery efficiency [15]. The article is structured as follows: first, the methodology is reviewed; next, results are presented from multiple simulations of drug delivery to a solid tumour growing into a vascularized host tissue, and concurrently, we discuss the implications of our predictions in the context of optimal drug delivery.

2. Material and methods

The present *in silico* cancer modelling methodology is motivated by the tumour growth and angiogenesis model proposed by the authors in [13]; hence, we have adopted here the same notation convention for the presentation of the mathematical models. The *in silico* cancer modelling framework consists of three interconnected core compartments that encompass different aspects of the mechano-biology of the cancerous and the host tissue, with one sub-compartment and one super-compartment that encapsulates all compartments. The core compartments of the framework are the *Solid mechanics*, the *Fluid mechanics* and the *Biochemics* compartments; whereas, the single sub-compartment of the framework is the *Drug delivery* one, which impacts the behaviour of the *Solid mechanics* and the *Biochemics* compartments.

Finally, the *Microvasculature/Angiogenesis* compartment is the super-set of all three core compartments, since blood vessels' structural integrity, perfusion state and ability to branch or/and elongate are affected by both biomechanical and biochemical factors. Figure 1 depicts via a flow chart of the aforementioned compartments of the proposed *in silico* framework, which are briefly presented in the following subsections.

2.1. Biochemical model compartment

The *Biochemics* model encompasses key biological factors associated with the development of a solid tumour and angiogenesis. These include the transport of oxygen and nutrients in the ECM, ξ, the transport of enzymes that degrade the ECM, μ, the balance of tumour-secreted angiogenic factors, τ, and the density of the ECM to connective (structural) tumour/host tissue, ϵ. The governing equations necessary to describe the first three state variables are defined in detail in [13] (see eqns (12)–(14) therein)—they are unaffected by the addition of the *Drug delivery* sub-compartment presented in §2.3.2. However, the balance equation of ϵ that describes the dynamics of the ECM is directly influenced by the drug agent, thus eqn (1) in [13] is modified to reflect this:

$$\dot{\epsilon} = \lambda_\epsilon \xi \, \mathrm{e}^{-\epsilon/\bar{\epsilon}} - \delta_\epsilon \mu \epsilon - \delta_\mathrm{d} c_\mathrm{i}^{\bar{\alpha}} \epsilon, \tag{2.1}$$

with the first term describing the rate at which ECM remodels, where the dot denotes time derivative, $\bar{\epsilon}$ is a scaling parameter that modulates the ECM level at which natural remodelling of the host-tissue matrix occurs and λ_ϵ an ECM-remodelling rate parameter. The last two terms in the previous equation describe the ECM degradation due to the presence of matrix-degrading enzymes—secreted by the tumour and the tip-endothelial cells of the tumour vasculature—and the effect of the drugs on the tumour cells' killing, with δ_ϵ and δ_d being the degradation rates, respectively. Also, c_i denotes the drug concentration that has internalized into the cancer cells of the tumour, as clarified in the following subsection, while $\bar{\alpha}$ is a model parameter that controls the cancerous tissue regression.

All continuity equations were discretized using linear finite elements, where we adopted a hexahedral-dominant grid, with zero flux set to all external boundaries for all variables. Numerical solution to the time-dependent equations has been carried out using an explicit time integration scheme, where zero initial values were set for state variables μ and τ while the distribution of ξ and ϵ was set uniform everywhere in the domain of analysis—to reflect physiological conditions prior to vascularized tumour growth.

2.2. Solid mechanics model compartment

The *Solid mechanics* compartment encompasses the biomechanics of the tumour and the host tissue, modelled here in three dimensions, and the biomechanics of the microvascular network. The balance of mechanical forces is expressed through the linear momentum equation—formulated in a Lagrangian framework, where both inertia and body forces are considered negligible:

$$\nabla \cdot [\mathbf{F} \cdot \mathbf{S}] = 0, \tag{2.2}$$

where $\mathbf{S}$ is the second Piola–Kirchhoff stress tensor. Following the multiplicative decomposition of the deformation gradient tensor into an elastic and an inelastic (growth) component respectively, as in [16]: $\mathbf{F} = \mathbf{F}_\mathrm{e} \cdot \mathbf{F}_\mathrm{g}$, where $\mathbf{F}_\mathrm{g} = (2\vartheta_\mathrm{g} + 1)^{1/2}\mathbf{I}$, with $\mathbf{I}$ the identity tensor and ϑ_g the volumetric deformation represented by the product of a Gompertzian growth function (expressed with respect to ξ) and a monomial function (expressed with respect to ϵ): $\vartheta_\mathrm{g} = \alpha_\mathrm{g}\{\exp[-\beta_\mathrm{g}\exp[-\gamma_\mathrm{g}\xi]] - \exp[-\beta_\mathrm{g}]\} \times \epsilon^{\delta_\mathrm{g}}$, where α_g, β_g, γ_g, δ_g are dimensionless parameters of the growth function. The constitutive equation of the tissue biomechanics is given by the general form [17] $\mathbf{S} = \partial\bar{W}/\partial\mathbf{E}_\mathrm{e}$, where $\mathbf{E}_\mathrm{e}$ is the elastic Green–Lagrange strain. The present model assumes a hyperelastic soft tissue biomechanics using the modified neo-Hookean stored energy function (see eqn (6.21) in [18]). From that equation, the structural integrity of the tissue is directly linked to the ECM-related state variable ϵ via $G(\epsilon) = \mu_\mathrm{e}\,\epsilon^{a_\mathrm{w}}$, where μ_e represents the material shear modulus, a_w (>0) is a constant parameter that modulates tissue softening/stiffening with respect to the ECM density.

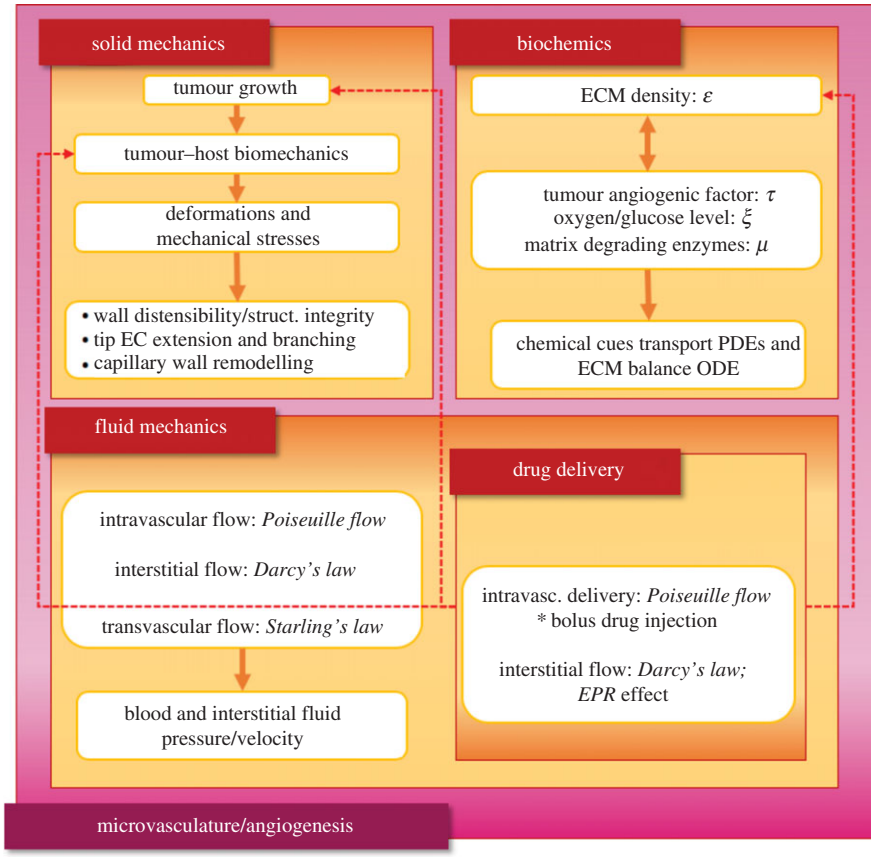

Figure 1. Graphical representation of the *in silico* cancer simulator, showing the core compartments of the coupled modelling approach. The framework consists of the solid mechanics compartment, the biochemics compartment and the fluid mechanics compartment, with the latter also encapsulating the drug delivery modelling component. (Online version in colour.)

The biomechanical interaction between the tumour–host biomechanics and the capillaries of the microvascular network and the corresponding biomechanical modelling of the capillary wall remodelling is thoroughly explained in our previous work [13]. As in that work, here the balance equation for the solid mechanics of the tumour and the host tissue has been discretized using finite elements. Numerical solution of the unknown displacements has been accomplished via a Newton–Raphson iterative scheme; this was necessitated by the presence of nonlinearities in the tissue biomechanics and the large deformations induced by the growing cancer mass.

2.3. Fluid mechanics model compartment

2.3.1. Microvascular and interstitial fluid flow

Microvascular haemodynamics is taken to obey the Hagen–Poiseuille law, where the capillary blood flow is assumed axial, steady, laminar and viscous [19]. Thus, the flow rate is given by $\dot{Q}_{\mathrm{vsc}} = -\pi R^4 \Delta p_{\mathrm{vsc}}/(8\,\mu_{\mathrm{B}}\,L_{\mathrm{vsc}})$, where R is the capillary lumen radius, Δp_{vsc} the vascular pressure drop within a capillary segment, L_{vsc}, and μ_{B} the dynamic viscosity of blood which is assumed homogeneous and constant in time. As in [13], the interstitial space is modelled as a porous biofluid-saturated medium, and interstitial fluid flow is modelled using Darcy's law. Thus, the flow rate at the interstitium is given by [1] $\dot{Q}_{\mathrm{int}} = -K_{\mathrm{int}} A_{\mathrm{int}} \Delta p_{\mathrm{int}}/L_{\mathrm{int}}$, where K_{int} and L_{int} are the average hydraulic conductivity and the relative distance between two material points in the interstitium whose (interstitial fluid) pressure difference is denoted by Δp_{int}, while A_{int} denotes the cross-sectional area of the interstitium. Finally, biofluid transport across the endothelium of the capillaries is modelled using Starling's law [12], with the transvascular flow rate expressed by $\dot{Q}_{\mathrm{trv}} = K_{\mathrm{vsc}} A_{\mathrm{vsc}} \Delta p_{\mathrm{v\text{-}i}}$, where A_{vsc} is the surface area of the blood vessel wall, $\Delta p_{\mathrm{v\text{-}i}}$ is the difference between the vascular and interstitial pressure. Also, K_{vsc} is the hydraulic conductivity of the endothelium and can be expressed as a function of the size of the pores size, r_{p}, the fraction of vessel wall surface occupied by pores, γ_{p}, the thickness of the vascular wall, h, and the plasma dynamic viscosity, μ_{P}, via [20] $K_{\mathrm{vsc}} = \gamma_{\mathrm{p}}\, r_{\mathrm{p}}^2/(8\mu_{\mathrm{P}}h)$.

All three flow-rate equations are coupled together in a model for the vascular and interstitial pressures that is formulated as a linear system of equations expressed at the vascular nodes of the network and the interstitial nodes of the three-dimensional finite-element grid (see figure 2). Also, an interconnected grid of tissue and vascular nodes is considered to bridge the two non-conforming meshes, hence, model flow between the vascular and interstitial (extravascular) space. Biofluid flow is solved numerically for the vascular and interstitial pressures while proper pressure/flow boundary conditions are applied on the terminal nodal points of the discretized domains. For more details about the boundary and initial conditions considered in this model, the reader should refer to our previous work [13].

2.3.2. Drug delivery

The continuity equation for the drug concentration in the bloodstream, c_{v}, is given from [1,19]

$$\dot{c}_{\mathrm{v}} + \boldsymbol{v}_{\mathrm{vsc}} \cdot \nabla c_{\mathrm{v}} = 0, \tag{2.3}$$

where the blood mean velocity, $\boldsymbol{v}_{\mathrm{vsc}}$, is computed after solving the equations governing the intra-, trans- and extravascular flow (as explained above).

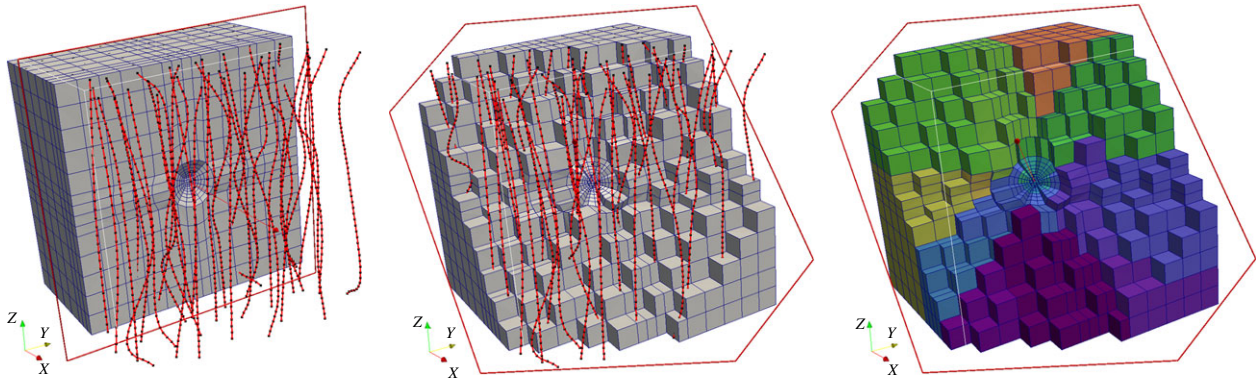

Figure 2. Cut-through of the three-dimensional finite-element mesh used to discretize the tumour and the host tissue (volume of analysed domain = 1.2 cm^3). The solid red lines depict the idealized vascular network used in the simulations (black dots correspond to the vascular nodes) which is relatively evenly distributed in three-dimensional space. Note that the two model discretizations are non-conforming. On the right, the colouring of the hexahedral elements demonstrates the visible partitions of the mesh, as decomposed for the purposes of the scalable *in silico* executions. (Online version in colour.)

Following [21], the drug in the extravascular space is identified in three discrete states: (i) the free-drug state, (ii) the bound-drug state and (iii) the internalized drug state, with their concentrations symbolized as c_f, c_b and c_i respectively. The balance of the free-drug concentration, c_f, is described via the advection–diffusion–reaction equation [12]

$$\dot{c}_f + \boldsymbol{v}_{int} \cdot \nabla c_f - \nabla \cdot [\mathbf{D}_f \cdot \nabla c_f] = \Phi_{vsc} + \Phi_{lmp} - k_{on} \bar{\epsilon}^{\bar{\beta}} c_f + k_{off} c_b - \delta_f c_f, \tag{2.4}$$

while the mass balance of the other two variables is described through a pair of ordinary differential equations

$$\dot{c}_b = k_{on} \bar{\epsilon}^{\bar{\beta}} c_f - k_{off} c_b - k_{int} c_b \tag{2.5}$$

and

$$\dot{c}_i = k_{int}\, c_b - \delta_i c_i, \tag{2.6}$$

where $\boldsymbol{v}_{int}$ is the interstitial fluid velocity vector (calculated through Darcy's law after evaluating p_{int}; see §2.3.1) and $\bar{\beta}$ is a model parameter that controls the drug association to the cancerous cells. The diffusion tensor of the drug molecule or drug-borne nanoparticle is $\mathbf{D}_f$ (assumed here isotropic, i.e. $= D_d \mathbf{I}$), while k_{on}, k_{off} and k_{int} are the association (binding), disassociation and internalization rate coefficients, respectively, and δ_f / δ_i is the half-life of the free drug and the decay rate of the drug—owing to the depletion of the cancer cells after the drug has found its target and the drug natural decay—respectively. The last two source terms in equation (2.4) come from the contribution of the vascular and the lymphatic network. Using Starling's law, the rate of solute transport per unit volume through the microvascular endothelial wall can be expressed as [22] $\Phi_{vsc} = P_{vsc,d} S_{vsc} (c_v - c_f) + K_{vsc}\, S_{vsc}\, (1 - \sigma_{f,vsc})\, \Delta p_{v\text{-}ic}$, where $c = c_v$ if $p_{vsc} > p_{int}$, else $c = c_f$; lymphatics contribution is expressed as $\Phi_{lmp} = K_{lmp} S_{lmp} (1 - \sigma_{f,lmp})(p_{lmp} - p_{int}) c_f$, where $P_{vsc,d}$ is the diffusive permeability of the blood vessels with respect to the solvent (drug molecule), K_{lmp} the hydraulic permeability of the lymphs' wall and $\sigma_{f,vsc} / \sigma_{f,lmp}$ the solvent drag reflection coefficient at the blood vessel/lymphatic wall. Both latter quantities can be estimated numerically as a function of the drug size to the size of the pores of the vessel wall [20], while S_{vsc} is microvascular density, i.e. the vessels' surface area per unit volume of tissue, and S_{lmp} the lymphatic vessels' density. For simplicity, the fluid pressure at the lymphatic vessels is assumed $p_{lmp} = 0$ everywhere in the domain of analysis.

Assuming the absence of interactions of the free drug with other macromolecules or/and enzymes, drug diffusion is controlled by the size of the drug; thus, it can be described through the Stokes–Einstein equation [23]—valid for when modelling chemotherapy transport: $D_d = k_B\, T / (3\pi \mu_l s_c)$, where k_B the Boltzmann constant, T the absolute (reference) temperature and s_c the size of the molecule (or hydrodynamic diameter if assumed spherical) of the free drug. However, for rigid particles (e.g. polymer vesicles, nanoparticles), Phillips *et al.* [24] proposed a modified diffusion formula that accounts for the hydrodynamic interactions of the drug with a fibrous matrix (here the collagenous matrix of the host stroma) that reads $D_d = D_0 / (1 + \sqrt{3 r_c} + r_c)$; D_0 is calculated from the previous equation, $r_c = s_c^2 / 3\kappa$, while the matrix permeability, κ, can be expressed with respect to the hydrodynamic diameter of the free drug and the porosity of the ECM, ε_s, through $\kappa = \varepsilon_s\, s_c / k_Y$, with k_Y being the Kozeny factor [25].

Equation (2.3) is discretized using two-node line elements that represent blood vessel segments of the microvascular network. For the outlet boundary nodes, zero-flux outflow condition is prescribed, i.e. $dc_v / dL = 0$, while for the inlet boundary nodes, c_v is prescribed explicitly to effectively model bolus injection of the drug through the exponential decay function: $c_v(t) = c_{v\text{-}max} \exp[-t/\tau_c]$, where $c_{v\text{-}max}$ is the maximum dose concentration of the drug that has reached the microcirculation system at the tumour site and τ_c the half-time of the drug. Similarly to the *Biochemics* model, differential equations (2.4)–(2.6) were discretized using the same finite element grid while time integration was accomplished via the forward Euler method using a 'lumped mass' capacity matrix to substantially speed up the numerical simulations.

2.4. Microvasculature/Angiogenesis compartment

A detailed description of this compartment can be found in the methodology description in [13]; here we present a brief overview. The *Microvasculature/Angiogenesis* compartment encompasses: (a) the elongation and extension of the tip capillary branches, the sprouting of existing blood vessels and the formation of vascular anastomoses, and (b) the remodelling of the capillaries' endothelial wall, the lumen size, the thickness of the wall, and the structural integrity of the vessels. As explained in the *Bioechemics* model above, the drug permits degrading the ECM only, whereas pruning of tumour vessels, disruption of the vascular remodelling, or modulation of the permeation of the endothelium is not accounted for in the present *in silico* framework; we leave this for future work.

2.5. Cancer model solution strategy

Numerical solution of the different compartments (as shown in figure 1) of the proposed *in silico* cancer modelling framework is accomplished in a staggered manner. The solution strategy employs five different time discretization scales, with each core or sub-compartment having a separate timestep. We iterate in time and we solve the equations involved in each

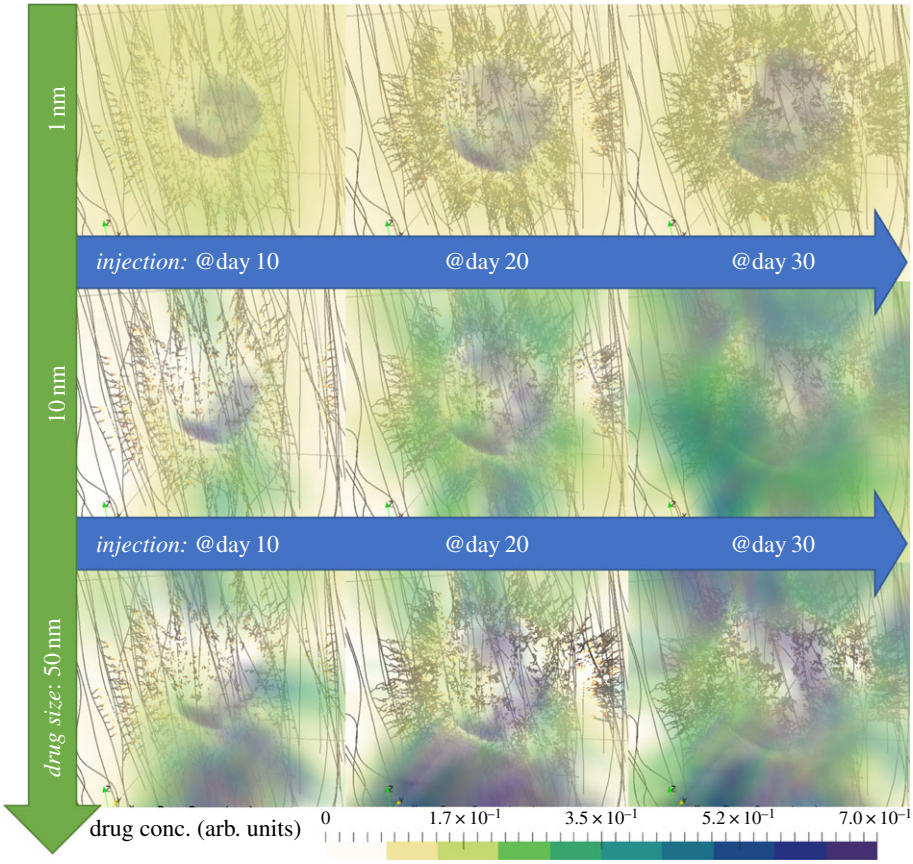

Figure 3. Snapshots of the *in silico* predicted drug distribution for the three drug cases (in rows). Each column corresponds to time-instants of tumour response to treatment 5 days after the time of drug injection. All simulation results correspond to the high porosity extracellular matrix case. The coloured cloud represents the drug concentration (as a fraction of the total drug administered) that has been associated with the tumour and the host tissue. For illustration purposes, the internal structure of the three-dimensional domain of analysis is transparent, while the microvascular network is coloured such that the well-perfused vessels are shown dark whereas the poorly perfused vessels are lightly coloured. (Online version in colour.)

compartment based on the timestep adopted for each one of them. Firstly, the balance equations for the *Biochemics* compartment are solved numerically, the solution of which is projected into the *Solid mechanics* compartment. Secondly, equilibrium is sought numerically in the *Solid mechanics* compartment, and then the numerical solution (strain, stress) is projected into the *Microvasculature/Angiogenesis*. At this point, within *Microvasculature/Angiogenesis*, the structural integrity of the vessels is evaluated and the tree is updated (i.e. sprouting, branching, vessel compression, etc.) accordingly. Subsequently, the flow equations of the *Fluid mechanics* compartment are solved to compute interstitial, intra- and transvascular flow (eqns (2)–(4) in [14]); then equations (2.3)–(2.6) of the *Drug delivery* subcompartment are solved to compute drug concentrations, the solution of which is distributed in the *Biochemics* and *Solid mechanics* models. The above steps are repeated until the simulation time has reached the desired end time point. However, it is important to highlight here that—regardless of the timestep adopted for the *Solid/Fluid mechanics* and *Microvasculature/Angiogenesis* compartments respectively—after solving the solid mechanics equations we enforce checking the vascular integrity, and subsequently the (bio)fluid flow equations are solved.

3. Results

We run simulations of tumour growth to replicate the development of a mammary carcinoma xenograft in immunodeficient mice [16]. In this study, we employed data of an *in vivo* murine syngeneic mammary MCaIV adenocarcinoma, as in [26,27]. The *in silico* cancer growth and angiogenesis model has been tested and validated in our previous paper [13]. Here, we model and simulate the single-dose administration of cancer cell killing drugs. The drugs investigated here varied with respect to their hydrodynamic size, i.e. the molecule/particle diameter was set approximately equal to 1 nm, 10 nm and 50 nm in order to mimic chemotherapy and nanomedicine transport in the animal model, respectively. All drugs were assumed to possess identical pharmacokinetic properties, i.e. excretion, absorption, internalization, decay. To simplify this study, the amount of *in silico* intravenous administration of the chemical was set the same for all drugs. We note, however, that this assumption is not representative of experimental protocols using laboratory mice; usually, the amount of drug administered varies with respect to the type of the drug. For example, administration of doxorubicin can span between 3 and 8 mg kg^{-1} while for nanoparticles this can vary from greater than 10 mg kg^{-1} [28]. The sole parameter that varied with respect to the drug pharmacokinetics was the half-time of the drug, τ_c, and was set based on experimentally measured clearance and drug circulation times in the bloodstream: 4 h, 10 h and 16 h, respectively [26]. In view of modelling flow in the capillaries using Poiseuille's law and the inflow/outflow boundary conditions considered in the simulations, the numerically evaluated average blood flow rate at the healthy capillaries is approximately 2.5 $cm^3\,h^{-1}$. Thus, the amount of drug

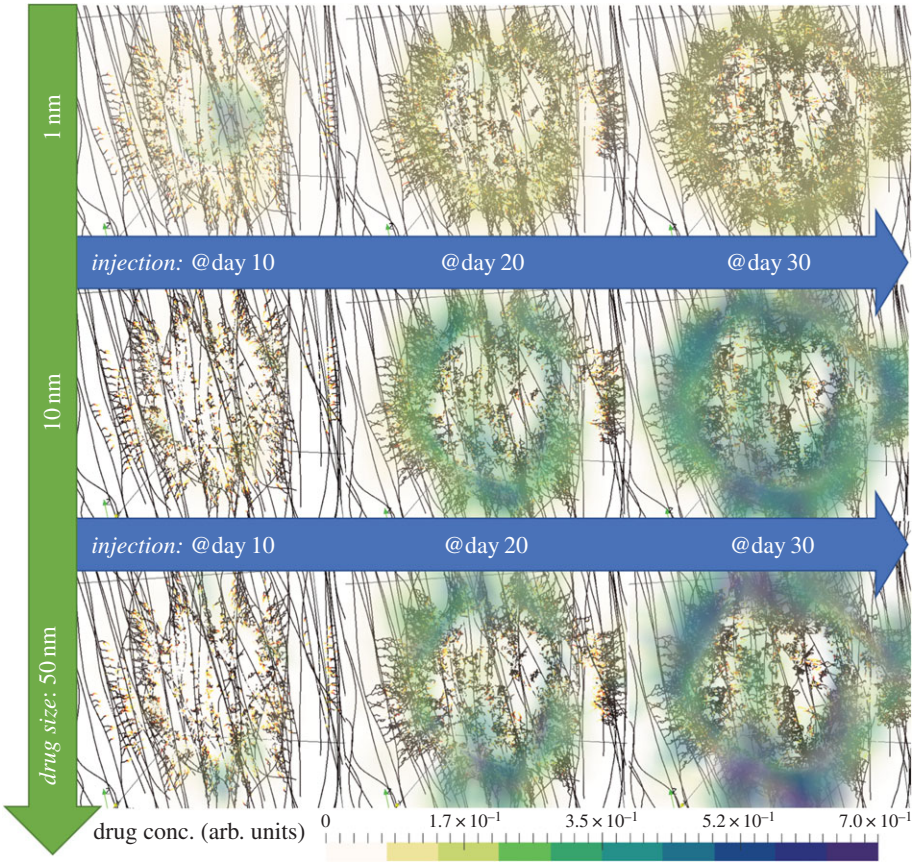

Figure 4. Snapshots of the *in silico* predicted drug distribution and the microvascular network for the three drug cases (in rows) and for the three injection times (in columns). All simulation results correspond to the low porosity extracellular matrix case. For detailed interpretation of the graphics, the reader is referred to the caption of figure 3. (Online version in colour.)

supplied over the period of the time-window of observation of the tumour development corresponded to 10, 25 and 40 times the maximum (intravenous) dose concentration of the drug, c_{v-max}.

Furthermore, in order to investigate the relationship between drug size and interstitial tissue hydraulic conductivity, simulations were also conducted with two different ECM hydraulic permeabilities: $\kappa = 6.4 \times 10^{-15}\ \mathrm{m}^2\ (\mathrm{Pa\ s})^{-1}$, henceforth termed 'high porosity'; and $\kappa = 6.4 \times 10^{-16}\ \mathrm{m}^2\ (\mathrm{Pa\ s})^{-1}$, henceforth termed 'low porosity'.

The model parameters required to simulate drug transport from equations (2.4)–(2.6) were taken from relevant works in the literature (e.g. [12,29]). We note that the adopted model parameters for the *Solid mechanics*, *Fluid mechanics* and *Biochemics* compartments are summarized in the electronic supplementary material. All simulations were carried out using our in-house developed *in silico* modelling framework—details about the numerical implementation of the framework are provided in the electronic supplementary material of our previous paper [14]. The C++ code of the *in silico* framework can be accessed online from the Bitbucket project: *Finite Element Bioengineering in 3D* (FEB3).

3.1. Drug size and interstitial porosity affects spatial distribution of delivery

Images of the predicted spatial distribution of the three drugs after single-dose injections at days 10, 20 and 30 are shown in figures 3 and 4, for high porosity and low porosity, respectively. Clear differences are observed between the two porosities, for all drug sizes; for high ECM porosity, the drug concentration is higher both inside and outside the tumour, while for low ECM porosity, the drug concentration is lower and approximately uniform throughout the volume (see electronic supplementary material, figure S1). Interestingly, both porosities produce an approximately uniform distribution of the cytotoxic drug (1 nm), but a highly heterogeneous distribution of the larger drugs (10 and 50 nm). This heterogeneity is driven by the spatially and time varying interstitial fluid velocity field in the ECM (see electronic supplementary material, figure S2), upon which the larger drugs are more dependent due to their motion being primarily governed by convective motion [3]. The accumulation of large molecules, such as nanoparticles, in non-tumour tissue is a hallmark of the enhanced permeability and retention (EPR) effect, a topic of heated debate [30,31].

3.2. Nanoparticles require high interstitial porosity to reduce tumour volume

To test the relationship between drug delivery efficacy and ECM hydraulic conductivity, figure 5 shows tumour volume over time for the control case and injections at days 10, 20 and 30, for each drug type, for high porosity (left column), and low porosity (right column) ECMs. A clear dependency of efficacy on porosity is observed, with low porosity reducing the efficacy of all three drug types. However, the cytotoxic drug (1 nm) is able to regress the tumour at both porosities, while the nanoparticles (10 and 50 nm) require high porosity to cause tumour regression; at low porosity, only the rate of growth is affected, and for the largest nanoparticle the effect

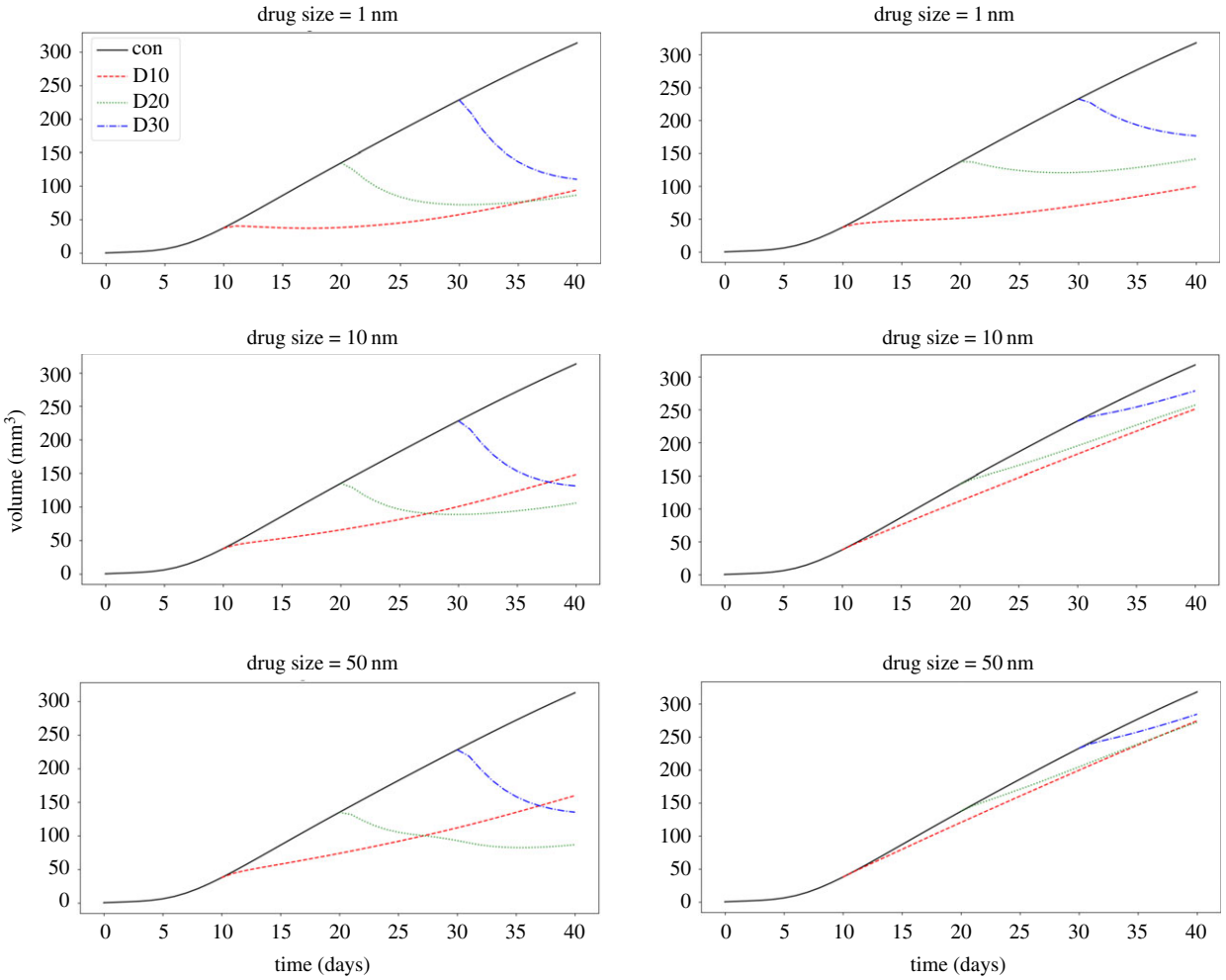

Figure 5. Line plots of the relative tumour volume (V = Vol.(t)/Vol.(t = 0) − 1) versus time, for control simulations (black solid lines), and treatments administered at days 10, 20 and 30 (D10, D20, D30; coloured dashed lines). The results in the left column correspond to high hydraulic conductivity ('high porosity'), K_{int}, and the results in the right column correspond to low hydraulic conductivity ('low porosity'). (Online version in colour.)

is almost negligible. This prediction recapitulates experimental observations of improved delivery efficacy as a result of ECM-modifying treatment with the anti-fibrotic drug tranilast; specifically, that reducing matrix density—or, equivalently, increasing matrix porosity—improves delivery of drugs in a size-independent manner [32]. It has been also documented that drugs targeting ECM-remodelling enzymes, such as FAK and hyaluronidase inhibitors, effectively slow tumour growth [33]. A similar effect was also observed with a cytotoxic drug when reducing the concentration of the high molecular weight glycosaminoglycan hyaluronan and hence increasing matrix porosity [34]. Here, we further predict that there is a regime where cytotoxics are effective, but not nanoparticles. Interestingly, the model also predicts that nanoparticles benefit from later injection times at high porosity; here this is due to the elevated interstitial fluid pressure produced by larger tumours increasing the magnitude of the convective flow. The phenomenon of growth-induced increases in interstitial fluid pressure has been previously reported in *in vivo* mouse experiments [35].

3.3. Transvascular velocity depends on both tissue porosity and drug size

The model was used to predict the transvascular fluid velocity, $\dot{Q}_{trv}$, for different drug types administered separately at days 10, 20 and 30, and for low and high EBM porosity. The resulting mean transvascular fluid velocity as a function of distance from the tumour centre is shown in figure 6, at 5 days (left column) and 10 days (right column) after the respective injection. For the earliest administration (day 10), the distribution is largely independent of drug type at both time points. However, for later administrations (days 20 and 30), there is a dependency of transvascular flow on both drug size and porosity, with low porosity producing a peak closer to the tumour centre than high porosity, and the cytoxic drug peaking closer to the tumour centre than the nanoparticles. This drives the porosity-dependent penetration of the drug observed in figures 3 and 4. Furthermore, the width of the distribution after cytotoxic drug delivery is predicted to be broader than after nanoparticle delivery, which suggests that a broader region of fluid pressure normalization is achieved after cytotoxic delivery. This supports our previous predictions of vascular network structure normalization by cytotoxic drug delivery [14], and given that the effects persist for at least 10 days after injection (as previously highlighted in terms of drug half-time), this prediction has implications for staged drug therapy.

4. Conclusion

Here we have described an *in silico* platform for quantitatively simulating the delivery of drugs of varying

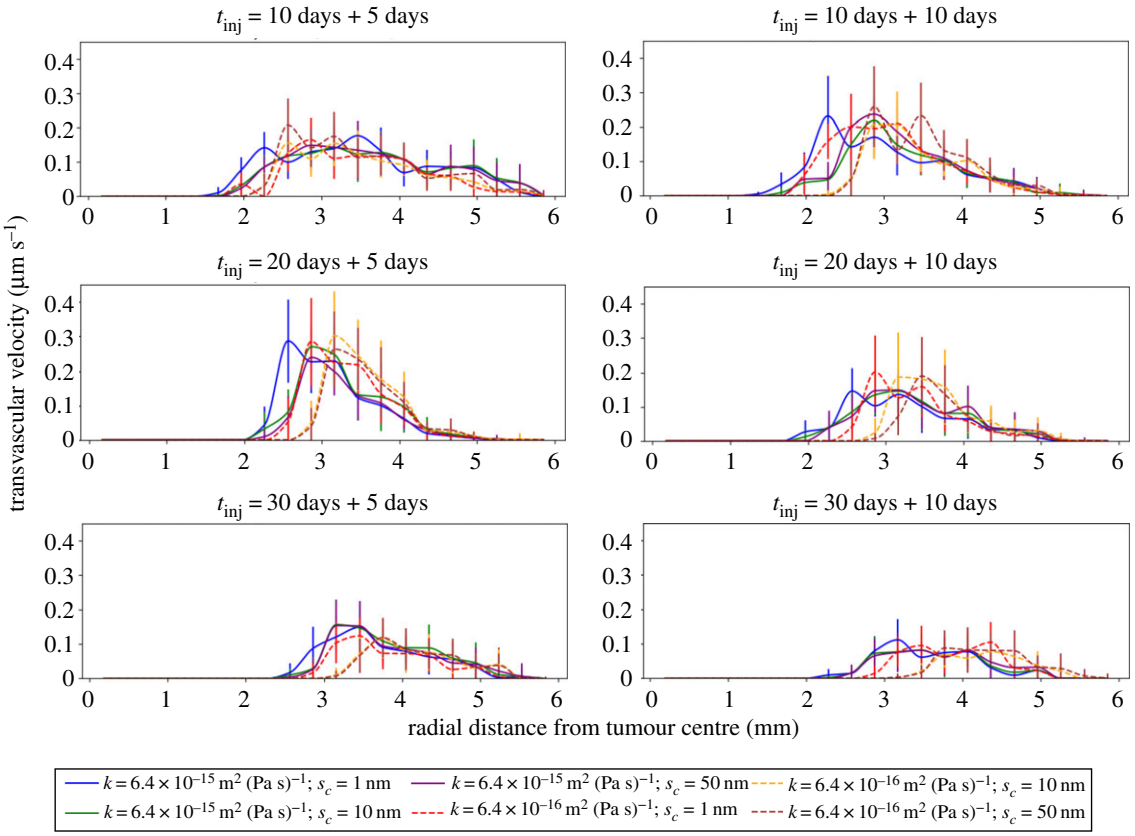

Figure 6. Line plots of the mean transvascular velocity (TRV) as a function of the radial distance from the centre of the tumour, with standard errors. Each row corresponds to a different time of injection, while each column depicts the TRV radial distribution 5 days and 10 days after drug administration. The legend lists the various simulation combinations based on the hydraulic conductivity of the ECM (κ) and the drug size (s_c). (Online version in colour.)

properties to a dynamically changing tumour–host environment. The proposed platform builds on our previous work [13,14] and generalizes to allow for both diffusive and convective transport mechanisms, hence enabling investigation into the dependency of delivery efficacy on drug size and extracellular matrix density. Future work will integrate our platform with multiscale methods [36] to test how host vasculature and tissue structure affect delivery efficacy of nanoparticles, and hence identify the optimal physiological conditions for size-dependent therapeutic drug delivery.

Data accessibility. The *in silico* platform can be accessed from the online repository on Bitbucket, FEB3: https://bitbucket.org/vasvav/feb3-finite-element-bioengineering-in-3d/wiki/Home.

Competing interests. We declare we have no competing interests.

Funding. P.A.W. and V.V. were financially supported by EPSRC-funded CMIC Platform Grants (project ID: EP/M020533/1; URL: https://gow.epsrc.ukri.org/NGBOViewGrant.aspx?GrantRef=EP/M020533/1).

References

1. Baxter LT, Jain RK. 1989 Transport of fluid and macromolecules in tumors. I. Role of interstitial pressure and convection. *Microvasc. Res.* **37**, 77–104. (doi:10.1016/0026-2862(89)90074-5)
2. Chauhan VP, Stylianopoulos T, Boucher Y, Jain RK. 2011 Delivery of molecular and nanoscale medicine to tumors: transport barriers and strategies. *Annu. Rev. Chem. Biomol. Eng.* **2**, 281–298. (doi:10.1146/annurev-chembioeng-061010-114300)
3. Dewhirst MW, Secomb TW. 2017 Transport of drugs from blood vessels to tumour tissue. *Nat. Rev. Cancer* **17**, 738–750. (doi:10.1038/nrc.2017.93)
4. Chen Q, Liu G, Liu S, Su H, Wang Y, Li J, Luo C. 2018 Remodeling the tumor microenvironment with emerging nanotherapeutics. *Trends Pharmacol. Sci.* **39**, 59–74. (doi:10.1016/j.tips.2017.10.009)
5. Netti PA, Baxter LT, Boucher Y, Skalak R, Jain RK. 1997 Macro- and microscopic fluid transport in living tissues: application to solid tumors. *AIChE J.* **43**, 818–834. (doi:10.1002/(ISSN)1547-5905)
6. Hobbs SK, Monsky WL, Yuan F, Roberts WG, Griffith L, Torchilin VP, Jain RK. 1998 Regulation of transport pathways in tumor vessels: role of tumor type and microenvironment. *Proc. Natl Acad. Sci. USA* **95**, 4607–4612. (doi:10.1073/pnas.95.8.4607)
7. Padera TP, Stoll BR, Tooredman JB, Capen D, di Tomaso E, Jain RK. 2004 Cancer cells compress intratumour vessels. *Nature* **427**, 695. (doi:10.1038/427695a)
8. Davis ME, Chen ZG, Shin DM. 2008 Nanoparticle therapeutics: an emerging treatment modality for cancer. *Nat. Rev. Drug Discov.* **7**, 771–782. (doi:10.1038/nrd2614)
9. Senthebane DA *et al.* 2017 The role of tumor microenvironment in chemoresistance: to survive, keep your enemies closer. *Int. J. Mol. Sci.* **18**, 1586. (doi:10.3390/ijms18071586)
10. Zhan W, Alamer M, Xu XY. 2018 Computational modelling of drug delivery to solid tumour: understanding the interplay between chemotherapeutics and biological system for optimised delivery systems. *Adv. Drug Deliv. Rev.* **132**, 81–103. (doi:10.1016/j.addr.2018.07.013)
11. D'Esposito A *et al.* 2018 Computational fluid dynamics with imaging of cleared tissue and of in vivo perfusion predicts drug uptake and treatment responses in tumours. *Nat. Biomed. Eng.* **2**, 773–787. (doi:10.1038/s41551-018-0306-y)
12. Sefidgar M, Soltani M, Raahemifar K, Sadeghi M, Bazmara H, Bazargan M, Mousavi Naeenian M. 2015 Numerical modeling of drug delivery in a dynamic solid tumor microvasculature. *Microvasc. Res.* **99**, 43–56. (doi:10.1016/j.mvr.2015.02.007)
13. Vavourakis V, Wijeratne PA, Shipley R, Loizidou M, Stylianopoulos T, Hawkes DJ. 2017 A validated

multiscale in-silico model for mechano-sensitive tumour angiogenesis and growth. *PLoS Comput. Biol.* **13**, e1005259. (doi:10.1371/journal.pcbi.1005259)

14. Vavourakis V, Stylianopoulos T, Wijeratne PA. 2018 In-silico dynamic analysis of cytotoxic drug administration to solid tumours: effect of binding affinity and vessel permeability. *PLoS Comput. Biol.* **14**, e1006460. (doi:10.1371/journal.pcbi.1006460)
15. Ledzewicz U, Schättler H. 2017 Application of mathematical models to metronomic chemotherapy: what can be inferred from minimal parameterized models? *Cancer Lett.* **401**, 74–80. (doi:10.1016/j.canlet.2017.03.021)
16. Wijeratne PA, Vavourakis V, Hipwell JH, Voutouri C, Papageorgis P, Stylianopoulos T, Evans A, Hawkes DJ. 2016 Multiscale modelling of solid tumour growth: the effect of collagen micromechanics. *Biomech. Model. Mechanobiol.* **15**, 1079–1090. (doi:10.1007/s10237-015-0745-2)
17. Holzapfel GA2000 *Nonlinear solid mechanics: a continuum approach for engineering*. Chichester, UK: Wiley.
18. Zienkiewicz OC, Taylor RL, Fox DD. 2014 *The finite element method for solid and structural mechanics*, 7th edn. Oxford, UK: Butterworth-Heinemann.
19. Pozrikidis C, Farrow DA. 2003 A model of fluid flow in solid tumors. *Ann. Biomed. Eng.* **31**, 181–194. (doi:10.1114/1.1540103)
20. Deen WM. 1987 Hindered transport of large molecules in liquid-filled pores. *AIChE J.* **33**, 1409–1425. (doi:10.1002/(ISSN)1547-5905)
21. Thurber GM, Wittrup KD. 2012 A mechanistic compartmental model for total antibody uptake in tumors. *J. Theor. Biol.* **314**, 57–68. (doi:10.1016/j.jtbi.2012.08.034)
22. Pietribiasi M, Waniewski J, Załuska A, Załuska W, Lindholm B. 2016 Modelling transcapillary transport of fluid and proteins in hemodialysis patients. *PLoS ONE* **11**, e0159748. (doi:10.1371/journal.pone.0159748)
23. Pluen A *et al.* 2001 Role of tumor-host interactions in interstitial diffusion of macromolecules: cranial vs. subcutaneous tumors. *Proc. Natl Acad. Sci. USA* **98**, 4628–4633. (doi:10.1073/pnas.081626898)
24. Phillips RJ, Deen WM, Brady JF. 1989 Hindered transport of spherical macromolecules in fibrous membranes and gels. *AIChE J.* **35**, 1761–1769. (doi:10.1002/(ISSN)1547-5905)
25. Pluen A, Netti PA, Jain RK, Berk DA. 1999 Diffusion of macromolecules in agarose gels: comparison of linear and globular configurations. *Biophys. J.* **77**, 542–552. (doi:10.1016/S0006-3495(99)76911-0)
26. Perrault SD, Walkey C, Jennings T, Fischer HC, Chan WCW. 2009 Mediating tumor targeting efficiency of nanoparticles through design. *Nano Lett.* **9**, 1909–1915. (doi:10.1021/nl900031y)
27. Vakoc BJ *et al.* 2009 Three-dimensional microscopy of the tumor microenvironment in vivo using optical frequency domain imaging. *Nat. Med.* **15**, 1219–1223. (doi:10.1038/nm.1971)
28. Chauhan VP, Stylianopoulos T, Martin JD, Popovic Z, Chen O, Kamoun WS, Bawendi MG, Fukumura D, Jain RK. 2012 Normalization of tumour blood vessels improves the delivery of nanomedicines in a size-dependent manner. *Nat. Nanotechnol.* **7**, 383–388. (doi:10.1038/nnano.2012.45)
29. Stylianopoulos T, Economides E-A, Baish JW, Fukumura D, Jain RK. 2015 Towards optimal design of cancer nanomedicines: multi-stage nanoparticles for the treatment of solid tumors. *Ann. Biomed. Eng.* **43**, 2291–2300. (doi:10.1007/s10439-015-1276-9)
30. Maeda H, Wu J, Sawa T, Matsumura Y, Hori K. 2000 Tumor vascular permeability and the EPR effect in macromolecular therapeutics: a review. *J. Control. Release* **65**, 271–284. (doi:10.1016/S0168-3659(99)00248-5)
31. Ojha T, Pathak V, Shi Y, Hennink WE, Moonen CTW, Storm G, Kiessling F, Lammers T. 2017 Pharmacological and physical vessel modulation strategies to improve EPR-mediated drug targeting to tumors. *Adv. Drug Deliv. Rev.* **119**, 44–60. (doi:10.1016/j.addr.2017.07.007)
32. Papageorgis P, Polydorou C, Mpekris F, Voutouri C, Agathokleous E, Kapnissi-Christodoulou CP, Stylianopoulos T. 2017 Tranilast-induced stress alleviation in solid tumors improves the efficacy of chemo- and nanotherapeutics in a size-independent manner. *Sci. Rep.* **7**, 46140. (doi:10.1038/srep46140)
33. Pickup MW, Mouw JK, Weaver VM. 2014 The extracellular matrix modulates the hallmarks of cancer. *EMBO Rep.* **15**, 1243–1253. (doi:10.15252/embr.201439246)
34. Kohli AG, Kivimäe S, Tiffany MR, Szoka FC. 2014 Improving the distribution of doxil in the tumor matrix by depletion of tumor hyaluronan. *J. Control. Release* **191**, 105–114. (doi:10.1016/j.jconrel.2014.05.019)
35. Boucher Y, Baxter LT, Jain RK. 1990 Interstitial pressure gradients in tissue-isolated and subcutaneous tumors: implications for therapy. *Cancer Res.* **50**, 4478–4484.
36. Wijeratne PA, Hipwell JH, Hawkes DJ, Stylianopoulos T, Vavourakis V. 2017 Multiscale biphasic modelling of peritumoural collagen microstructure: the effect of tumour growth on permeability and fluid flow. *PLoS ONE* **12**, e0184511. (doi:10.1371/journal.pone.0184511)